Available online at www.sciencedirect.com
SCIENCE DIRECT®
ELSEVIER
International Journal of Multiphase Flow 29 (2003) 1833–1856
International Journal of Multiphase Flow
www.elsevier.com/locate/ijmulflow

Dispersed multiphase flow with air-driven runback of a liquid layer at a moving boundary

G.F. Naterer *

Department of Mechanical and Industrial Engineering, University of Manitoba, 15 Gillson Street, Winnipeg, Manitoba, Canada R3T 2N2

Received 11 October 2002; received in revised form 1 October 2003

Abstract

Multiphase flow with impinging droplets on an icing surface with a flowing supercooled surface layer is investigated. The air-assisted flowing layer is modelled with the cross-phase shear stresses imparted at the moving liquid/air interface. Runback and runoff of the surface layer are predicted by mass flow across the boundaries between adjacent elements in the numerical formulation. This liquid runoff is determined by coupled heat and momentum balances for the unfrozen water layer. The numerical analysis is developed with a control-volume-based finite element method (CVFEM). An Eulerian formulation with volume averaging is developed to accommodate the near-wall elements containing both dispersed and continuous phases. The predicted results are successfully validated through comparisons with analytical solutions and measured data.

1. Introduction

Multiphase flow with droplets in three-phase conditions arises when impinging droplets on a moving phase interface lead to the formation of a surface liquid film. This type of multiphase flow occurs in various engineering instances. Some important examples include aircraft and power line icing, thermal spray coatings, thin laminations manufactured by uniform droplet spray (UDS) processes and droplet/wall interactions in combustion engines. For example, heat transfer during impingement of fuel spray droplets on the walls of a piston cavity affect the combustion process in DI diesel engines. In the icing examples, *rime ice* (or *dry ice*) occurs when incoming droplets are

* Tel.: +1-204-474-9804; fax: +1-204-275-7507.
E-mail address: natrerg@cc.umanitoba.ca (G.F. Naterer).

0301-9322/$ - see front matter © 2003 Elsevier Ltd. All rights reserved.
doi:10.1016/j.ijmultiphaseflow.2003.10.002

solidified immediately upon impact on the ice surface. Impinging droplets impart the latent heat of phase change upon solidification at the phase interface. This energy transfer and other heating modes may heat the ice surface sufficiently to sustain an unfrozen water layer. In that case, *glaze ice* (or *wet ice*) is formed, whereby growth of the ice and unfrozen water layer occur simultaneously.

Different regimes of runback flow of this supercooled water layer may occur on the glaze ice surface (Hansman et al., 1991). These regimes include (i) a smooth wet zone with a uniform water film, (ii) a rough zone with horn-shaped elements, (iii) another runback zone with rivulets and (iv) a dry zone with rime ice. In the rough zone, surface tension causes coalescence of unfrozen water into beads. The transition between smooth and rough zones may be related to the transition of the boundary layer from laminar to turbulent. The runback water often freezes after a short distance traveled downstream, where there is little or no droplet impingement and sufficient heat losses. Freezing of the runback water can produce horn-shaped structures, which characterize glaze ice (Kind, 1998). Stability of the adjacent air stream is affected by this runback flow (Tsao et al., 1997). Experimental studies involving icing of power lines have been presented by Lu et al. (1998), while Tsuboi and Kimura (1998) have predicted numerically the droplet flows around such conductors. The application of computational fluid dynamics (CFD) represents an important technology for overcoming problems arising from icing of aircraft and power lines.

This article will consider an extension of conventional two-fluid formulations to accommodate volume averaging of one dispersed phase (droplets) and three continuous phases (air, surface film, ice), simultaneously. The dynamic interactions between these phases are included through appropriate cross-phase interactions. An example is the interfacial resistance (drag) between the droplet and air phases. In this Eulerian type method, reduced computational costs (time and storage) can be realized, while effectively retaining the appropriate thermal and fluid physics through the cross-phase interactions. This approach allows the droplet flow equations to be expressed in a standard scalar transport form on a fixed grid. In this article, these equations for impinging droplets and glaze ice growth will be established by a volume averaging procedure.

During glaze ice growth, the impinging droplets arrive on the flowing supercooled surface film. This unfrozen layer of water along the ice surface can contribute appreciably to the dynamics of glaze ice buildup. The radial flow of a thin fluid layer, under the influence of Coriolis, centrifugal, gravity and surface tension forces was predicted numerically by Myers and Charpin (2000). Under certain conditions, the velocity equations become de-coupled and the effects of Coriolis forces on the film height become negligible. For tension-driven flows of thin films, traveling waves and slip conditions at the free surface can be modelled by higher-order differential equations (Myers, 1998). Analytical modeling of glaze ice involves coupled heat and momentum balances in the unfrozen water layer (Poots, 1996). The dynamics of the flowing supercooled water film has been documented by Karev and Farzaneh (2001). This issue has also been dealt with specifically for steady state conditions (Poots, 1996), shear driven film flow (Bourgault et al., 2000) and general modelling (Myers et al., 2002). Hedde and Guffond (1992) predict a glaze ice accretion numerically through a grid deformation. In this approach, a new grid is generated in the runback direction along the glaze ice surface, or by interpolating the rate of icing on the original mesh. The ice height is calculated based on the icing rate multiplied by the time step.

In this article, a new three-phase formulation involving film flow of the water layer will be presented. This formulation is based on previous studies involving glaze ice heat transfer (Mes-

singer, 1953; Naterer, 2002a; Myers and Hammond, 1999), as well as extensions of previous finite element modeling of rime ice growth (Naterer, 2002b). Rather than explicitly resolving the droplet trajectories (Lagrangian approach) or film interface location (interface tracking method), this work uses volume averaging (Eulerian method) to predict the surface film flow. The goal of such modeling is to yield computational savings, in terms of time and storage, due to the volume averaging procedures therein. It is shown that such averaging properly accommodates the inter-phase processes (lost through the averaging) with appropriate cross-phase interactions supplied thereafter. Predicted results involving ice buildup are successfully compared with analytical and experimental data.

2. Problem formulation

In the current Eulerian formulation, the multiphase equations will be determined by spatial averaging of the individual phase equations, within a control volume containing multiple phases. These phases may include gas (air), liquid (droplets and/or unfrozen water layer) and solid (ice) phases, simultaneously. For example, impinging supercooled droplets arrive on the advancing ice boundary, which is covered by a flowing supercooled layer of water (see Fig. 1). Additional cross-phase interactions must be supplied, due to information lost at the interfacial boundaries in the volume averaging. In this section, this volume averaging procedure will be described.

2.1. General scalar conservation equation

The conservation form of the governing equation for a scalar quantity, ϕ_k, associated with phase k in a multiphase mixture, is determined from volume averaging over a differential control volume (Banerjee and Chan, 1980). In this article, $k = 1$ refers to the dispersed phase (droplets), while $k = 2$ refers to the carrier phase of the air stream. In the near-wall region, the subscript k would cover three different phases, namely gas (air), liquid (droplets and/or surface film) and solid (ice) phases.

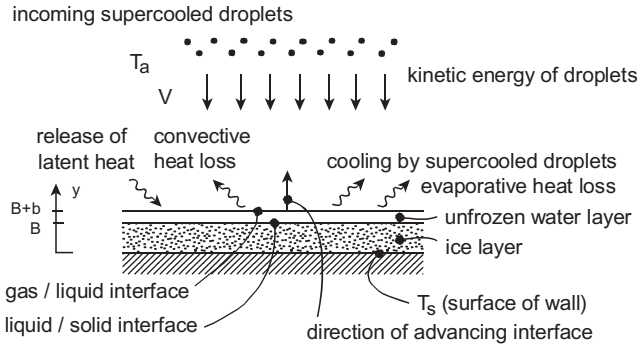

Fig. 1. Glaze ice with unfrozen water layer.

When applying spatial averaging to the dispersed (droplet) phase, the predicted results will give a volume averaged representation for the behaviour of multiple droplets within a control volume. Certain microscopic information is lost in this averaging procedure. Information lost at the interfacial boundaries is re-supplied through constituitive relations. In this article, a volume averaged quantity, $\langle \alpha_k \rangle$, and volume fraction of phase k (used as a subscript), denoted by C_k, are defined as follows:

$$\langle \alpha_k \rangle = \frac{1}{V_k} \int_{V_k} \alpha_k \, \mathrm{d}V \tag{1}$$

$$C_k = \frac{V_k}{V} \tag{2}$$

Based on volume averaging of the differential scalar conservation equation (Banerjee and Chan, 1980),

$$\frac{\partial}{\partial t} C_k \langle \rho_k \phi_k \rangle + \frac{\partial}{\partial x} C_k \left\langle \hat{n}_x \cdot (\rho_k \phi_k \mathbf{v}_k + \mathbf{j}_k) \right\rangle + \frac{1}{V} \int_a \left(\dot{m}''_k \phi_k + \mathbf{j}_k \cdot \hat{n}_k \right) \mathrm{d}S = C_k \left\langle \hat{S}_k \right\rangle \tag{3}$$

This results represents a 1-D form of the equation, which can be readily extended to include multi-dimensionality. In Eq. (3), $\dot{m}''_k$ and $\mathbf{j}_k$ refer to the cross-phase mass flux (units of kg/m^2 s) and diffusive flux, respectively. Also, $\int_a$ refers to integration over the total area, including any area of phase k in contact with the external walls or boundaries, a_w, and the interfacial area per unit volume, a_i, i.e., along the boundary separating the phases. Based on Eq. (3), the mass and momentum equations of multiphase flow can be obtained. In the multi-dimensional form of Eq. (3), the dot products with $\hat{n}_y$ and $\hat{n}_z$, leading to y- and z-direction derivatives, respectively, would be included.

2.2. Mass equation

This equation will be written in terms of the *liquid water content*, $\widehat{\rho_l}$, which represents the mass of water (droplets) per unit volume of the water/air mixture. It is defined by

$$\hat{\rho}_l = \frac{m_l}{V} = C_k \langle \rho_k \rangle \tag{4}$$

The volume averaged form of the mass equation becomes (Banerjee and Chan, 1980)

$$\frac{\partial \hat{\rho}_l}{\partial t} + \frac{\partial (\hat{\rho}_l u_l)}{\partial x} + \frac{\partial (\hat{\rho}_l v_l)}{\partial y} = 0 \tag{5}$$

This equation will be solved analogously to a transport equation involving species concentration, whereby the ''concentration'' of droplets (or phase fraction) is tracked throughout the flow field. This concentration of the liquid phase is usually called the liquid water content (LWC) in the aircraft icing literature. The volume fraction of phase k, denoted by C_k, can be calculated in terms of $\hat{\rho}_l$ from Eq. (5) following multiplication by ρ_w (the density of water). In three-phase conditions, both liquid and solid fractions are required along the ice surface, since growth of ice and the unfrozen water layer may occur simultaneously.

2.3. Momentum equations

The volume averaged form of the x-direction momentum equation will be approximated as (Naterer, 2002b)

$$\frac{\partial(\hat{\rho}_l u_l)}{\partial t} + \frac{\partial(\hat{\rho}_l u_l u_l)}{\partial x} + \frac{\partial(\hat{\rho}_l u_l v_l)}{\partial y} + \langle \dot{m}_l'' u_l \rangle = C_l \langle G_{x,l} \rangle \tag{6}$$

An additional gravity term appears in the y-direction momentum equation, so that droplets fall under their own weight. The momentum equations for the carrier (air) phase are derived separately and resemble the single phase Navier–Stokes equations (Tsuboi and Kimura, 1998), except that cross-phase terms are included for interfacial resistance (drag) between the droplets and air. In the numerical formulation, the momentum equations are solved once $\hat{\rho}_l$ (or C_l) is obtained from Eq. (5).

In Eq. (6), the cross-phase interactions, $G_{x,k}$, are determined from an interfacial resistance law, based on correlations presented by Hewitt et al. (1997) and Tsuboi and Kimura (1998), with drag coefficients adopted as by Szilder et al. (1987). Such correlations can be expressed in terms of an inertia parameter and droplet freestream Reynolds number, based on the classic work of Langmuir and Blodgett (1946). The resulting equations govern the external flow, while additional near-wall equations are needed for the flowing supercooled surface layer. A thin film approximation is used for the momentum equation in this flowing surface layer (Poots, 1996). In an upcoming section, it will be shown that this approximation leads to a linear velocity profile within the unfrozen water layer. Once this velocity profile is determined, the mass outflow from a control volume due to surface runback can be determined. This runback flow of unfrozen water gives the portion of liquid mass transferred between elements along the moving boundary of the ice surface.

2.4. Additional real-world complexities

Before an ice accretion model can be applied to actual problems such as aircraft icing, additional real-world complexities must be considered, such as roughness and surface vibrations. Although detailed modelling of these factors is beyond the scope of the current article, their general impact should be considered. The purpose of this section is to give a brief physical outline of some examples, with some indication of how the numerical model could be extended to accommodate them.

For example, the impact of ice surface roughness on the convective heat transfer and friction coefficients has been developed based on a momentum integral equation in Appendix A.3. However, for more generally derived profiles of the near-wall velocity or temperature distribution, as needed in calculations such as turbulence transition, a damping effect of roughness based on the Van Driest profile (1956) can be adopted (Hedde and Guffond, 1992). The icing surface often contains discrete zones along the surface, which exhibit varying surface roughness. Close to the stagnation point of the body, the icing surface is often smooth and uniformly wet (Hansman et al., 1991). Following the smooth zone, there is a transition to a rougher ice surface with insufficient water to maintain a uniform film. The runback water can coalesce into water beads, depending on local boundary layer transition to turbulence. The enhanced heat transfer due to turbulence causes sufficient freezing to partially dry the surface and cause the bead formation. In the current

article, a discrete transition is assumed from rime (dry) ice to glaze (wet) ice, considering a uniform water film without the bead formation.

The formation of transition beads at the smooth/rough interface affects the heat transfer within the rough zone, while initiating drying of the surface and freezing of the downstream beads. Some ice roughness elements can grow into distinct protrusions, under certain glaze ice conditions with high liquid water content (Hansman et al., 1991). If these elements extend far enough above the icing surface, they can lead to separate macroscopic horned ice accretions, which catch droplets that would otherwise have been swept away from the ice surface. This collected water can slowly freeze into rivulets or lead to other coalesced water cells. Although not modelled in the current work, a maximum stable droplet size for the roughness height within the horn zone could be utilized. Then, if the water layer in the control volume exceeds a maximum film thickness based on the impinging water content, the heat balance would suggest how much water would be shed from the surface to runback. Iteration would be required for convergence between the estimate of this parameter in the boundary layer model, and the increase of film thickness. Accurately predicting if/when ice sheds off from the surface is expected to require detailed understanding of these processes.

In addition to surface roughness, icing of the surface can produce dynamic forces that result in surface vibrations. Such vibrations add considerable complexity to the calculations, due to the simultaneous ice growth and time varying aerodynamic forces on the moving ice surface. In some icing conditions, these vibrations may become unstable, thereby leading to serious hardware damage. The flow induced vibrations lead to strong non-linearities in the governing equations. The oscillating position of the icing surface depends on the aerodynamic forces, while the flow past the ice surface is altered by the surface vibrations. A main parameter of interest required from the icing model is the net force arising from the flow past the ice surface. The surface vibrations lead to periodic trends of the drag and lift coefficients over time, due to processes such as vortex shedding and boundary layer separation. The aerodynamic forces arising from these vibrations can be predicted after the velocity, velocity gradient and pressure distributions are obtained from the CFD code. Then, a numerical method such as moving grid points or coordinate transformations would be needed for displacement of the icing surface due to the time-varying forces. Once the surface is displaced, the flow field prediction must be re-calculated, and iteration is needed until solution convergence is reached.

3. Numerical formulation

The numerical formulation is based on a hybrid finite element/volume method, as detailed elsewhere (Naterer, 2002b,c). In this section, the modeling of phase change of the impinging supercooled droplets, as well as the momentum equations and runback flow of the unfrozen water layer, will be described.

3.1. Modeling of phase change of incoming droplets

Based on Messinger (1953), the energy balance at the ice/air interface during rime ice growth is

$$q_k + q_l + q_a = q_{cond} + q_{conv} + q_d \tag{7}$$

The individual terms are given by the following heat fluxes (designated by q):

- $q_k = (\beta VG)V^2/2$; kinetic energy of impinging droplets,
- $q_l = \rho L(\partial B/\partial t)$; release of latent heat of fusion,
- $q_a = rhV^2/2c_p$; viscous heating (coefficients adopted as by Myers and Hammond, 1999),
- $q_{cond} = -k(\partial T/\partial n)$; rate of heat conduction through ice, unfrozen water layer,
- $q_d = \beta VGc_w(T_w - T_a)$; cooling by incoming supercooled droplets,
- $q_{conv} = h(T_w - T_a)$; convective heat loss,
- $q_{evap} = \chi_e e_0(T_w - T_a)$; evaporative heat loss.

These modes of energy exchange are illustrated in Fig. 1. The variables β, B, e_0, G, h, L and V refer to the collection efficiency, ice thickness, vapor pressure constant, liquid water content, convection coefficient, latent heat of fusion and velocity magnitude, respectively. During rime ice growth in Eq. (7), droplets are solidified immediately on impact, without a surface liquid film experiencing the evaporative heat loss. However, such evaporative heat losses occur from the surface of the unfrozen surface film, after transition to glaze ice. In that case, the evaporation energy term, q_{evap}, is included in Eq. (7).

After transition to glaze ice, only a fraction of the latent heat of incoming droplets is released, since some droplets remain in the surface liquid film. Based on Messinger (1953), this fraction can be determined by re-solving Eq. (7), in terms of the unknown proportion of latent heat released, n, i.e.,

$$n = \frac{1}{\beta VGL}\left\{k_i\left|\frac{\partial T}{\partial \hat{n}}\right| + h(T_f - T_a) + \beta VGc_w(T_f - T_a) + \chi_e e_0(T_f - T_a) - \frac{1}{2}GV^3\right\} \tag{8}$$

where $\hat{n}$ refers to the direction normal to the interface. The proportion, n, is illustrated in Fig. 2. It represents the fraction of energy required to raise the ice temperature up to T_f. The temperature of T_f refers to the freezing point (0 °C for water). Thus, it gives the fraction of impinging droplets which freeze on the ice surface. The remaining fraction, $1 - n$, stays in the liquid phase and flows in a thin layer along the ice surface. In Fig. 2, ip and SCV refer to integration point at the midpoint of each sub-surface, and sub-control volume, respectively.

In Eq. (8), a denominator of βVGL is obtained. From a mass balance of incoming droplets and growing ice and surface water, the fraction of incoming droplets which freeze, n, is the ice growth rate multiplied by $\rho_i/\beta VG$. Also, from a heat balance at the water/ice interface, the ice growth rate is determined from the difference between temperature gradients on both sides of the interface, multiplied by $k/\rho_i L$. Using the heat flows from Eq. (7) to represent the water temperature gradient, and combining the expressions, leads to the denominator of βVGL in Eq. (8). For the purpose of estimating n in Eq. (8), the approximation is made that the unfrozen water layer temperature, T_w, is about T_f (phase change temperature; 0 °C). This approach represents a quasi-isothermal film, since the terms of Eq. (8) are determined from a balance at the water/air interface, which includes the temperature gradient in the unfrozen water layer. It should be noted that the result in Eq. (8) has multi-dimensional applicability, unlike analytical solutions developed for certain circumstances, such as 1-D conditions.

An important component of Eq. (8) involves the estimation of the convective heat transfer coefficient, h. This coefficient can be determined after using the computed velocity field to solve

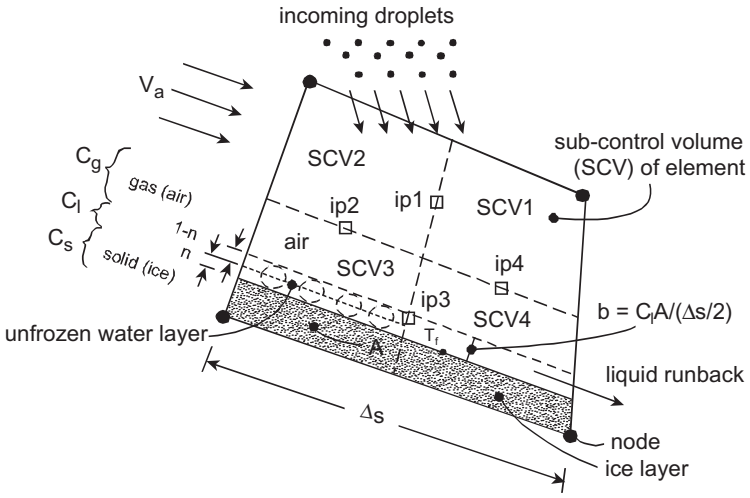

Fig. 2. Discretization with surface film flow.

the energy equation for temperature, particularly the local air temperature, T_a. Then, the Fourier heat flux in the fluid at the wall (subscript w) represents the computed heat transfer by convection due to Newton's Law of Cooling, i.e.,

$$-k\left.\frac{\partial T}{\partial y}\right|_w = h(T_w - T_a) \tag{9}$$

In this way, h can be determined once the grid is sufficiently refined within the boundary layer to accurately represent the wall temperature gradient. This approach involves a detailed near-wall grid refinement, as well as the wall temperature, which may be unknown. Also, modelling of incoming droplets at the moving solid/liquid interface would require re-meshing at every time step, in order to retain the mesh refinement in the boundary layer region of transient ice growth. These steps could entail significant computational costs, both in terms of time and storage.

As a result, an alternative approach is described here to approximate Eq. (9). For laminar flows (see Appendix A),

$$h(x) = 0.2926kv^{-0.5}\left\{u_\infty(x)^{-2.87}\int_0^S u_\infty(x)^{1.87}\,\mathrm{d}s\right\}^{-0.5} \tag{10}$$

where v and $u_\infty(x)$ represent the kinematic viscosity and the velocity component parallel to the wall outside of the boundary layer, respectively. For turbulent flows, the Stanton number, St, is written in terms of the Prandtl number, Pr, as follows:

$$St(x) = \frac{h(x)}{\rho c_p u_\infty(x)} = 0.0287Pr^{-0.4}\frac{(T_w - T_\infty)^{0.25}\mu^{0.2}}{\left[\int_0^x (T_w - T_\infty)^{1.25}\rho u_\infty\,\mathrm{d}x\right]^{0.2}} \tag{11}$$

Details regarding derivations of these results, together with their extension to rough surfaces arising during icing, are outlined in Appendix A. Additional details regarding their roles in the heat transfer modeling are documented by Naterer (2003).

3.2. Discretized momentum equation in the surface liquid layer

As described earlier, runback flow occurs in the unfrozen water layer during glaze ice conditions. Along the ice surface, impinging droplets impart latent heat into the surface while freezing, which generates and sustains the flowing supercooled surface film. During the glaze ice growth, a momentum balance within the surface film must be considered to predict the flow behaviour within the liquid layer. A thin film approximation will be used in this analysis (note: previously developed for icing problems by Poots, 1996). Furthermore, an energy balance in the liquid film involves the fraction of liquid leaving a finite volume and entering an adjacent control volume. If fewer or no droplets impinge on the surface, or insufficient heat is transferred into the ice surface, then the liquid layer may freeze and no longer flow along the ice surface.

In this article, a continuous layer of unfrozen water flows along the glaze ice surface. Such flowing supercooled water along an ice surface has been documented by Karev and Farzaneh (2001). In this work, it will be assumed that the unfrozen water layer is mainly driven by a constant shear stress, denoted by τ, applied to its outer edge by the adjacent airstream. From a scaling analysis under typical icing conditions, it can be shown that the dominant term in the streamwise film momentum equation is the cross-stream diffusion. In particular, the reduced x-momentum equation parallel to the ice surface for a sufficiently thin film becomes (Bourgault et al., 2000)

$$\frac{\partial^2 u}{\partial y^2} = 0 \tag{12}$$

which represents a quasi-steady result with a neglected streamwise pressure gradient within the liquid layer.

Various surface film regimes have been classified by Fulford (1964) based on the film Reynolds number, i.e.,

$$Re_b = \frac{\bar{u} b}{\nu_w} \tag{13}$$

where $\bar{u}$ and b refer to the mean velocity and local height of the water film, respectively. The transition Reynolds number from laminar to turbulent flow is $Re_b = 270$. A laminar regime is followed by laminar/wavy and turbulent regimes when the film Reynolds number increases. However, their detailed structures are affected by the impinging droplets in realistic icing conditions. Additional factors, such as instabilities of the advancing solid/liquid interface and shear-driven interaction of the free surface with droplets, render a detailed analysis difficult. In the current article, analogies to other similar film flows will be used as a basis from which the glaze icing can be analyzed.

Equation (12) is solved subject to the following boundary conditions:

$$\left.\frac{\partial u}{\partial y}\right|_{y=b} = \frac{\tau}{\rho_w \nu_w} \tag{14}$$

$$u(y=0) = 0 \tag{15}$$

to yield the following linear velocity profile in the unfrozen water layer,

$$u = \frac{\tau y}{\rho_w \nu_w} \tag{16}$$

This result has been derived in the same context by Bourgault et al. (2000), and a more general form by Myers et al. (2002). Integrating this profile across the thickness of the film yields the following mean velocity:

$$\bar{u} = \frac{1}{b}\int_0^b u\,dy = \frac{\tau b}{2\rho_w \nu_w} \tag{17}$$

which can be used to determine the film Reynolds number.

Based on experimental data for the shear stress at the water/air interface in the laminar regime (Cheremisinoff and Davis, 1979),

$$\tau = \frac{1}{2} f_i \rho_a V_a^2 \tag{18}$$

where V_a and f_i refer to the local air velocity and interfacial friction factor, respectively. The friction factor is different than the skin friction coefficient (usually denoted by c_f). The skin friction coefficient refers to flow along a stationary solid surface, while not accounting for the effects of shear action due to a moving surface film. Based on experimental data correlated by Cheremisinoff and Davis (1979),

$$f_i = 0.008 + (2 \times 10^{-5}) Re_b \tag{19}$$

Also, from experimental data in the turbulent regime (Cheremisinoff and Davis, 1979) , the interfacial shear stress is

$$\tau = \frac{4 \times 10^{-3} \cdot \rho_a V_a^2}{1 - 2 \times 10^{-5} \cdot b^2 \rho_a V_a^2 / (\rho_w \nu_w^2)} \tag{20}$$

A smooth free surface of unfrozen water, without surface waves, is idealized in these approximations. Physical data involving the detailed turbulence structure of surface films is limited, particularly in the presence of solid/liquid phase change and impinging droplets, as they occur in icing problems. There exists certain similarities between free surface flows in channels and wind-driven film flows. The dynamics of the processes in supercooled film flow have been outlined by Karev and Farzaneh (2001). Turbulent eddy motion near the outer free surface of a thin water film is expected to be suppressed by the ice surface, when compared with deep layers, including free channel flows. The wind-driven shear action imparts a momentum flux across the free surface which diffuses downwards through the supercooled water layer.

Within the unfrozen water layer, surface tension is expected to suppress turbulent velocity fluctuations normal to the free surface. When covered by a liquid layer, the glaze ice surface is

usually smooth. Thus, surface roughness is not expected to have appreciable impact on the turbulence, unlike rime ice which may involve considerable surface roughness. In that case, supercooled droplets freeze immediately on impact, thereby creating interspersed air/ice pockets and leading to roughness along the ice surface. In this article, the film flow is considered to occur along a smooth glaze ice surface. Its detailed interaction with the external flow can be predicted by a coupled Navier–Stokes solver in the surface film and external flow field. However, this iterative approach would entail considerable computational costs, partly due to adaptive re-meshing required at each time step. The following section develops an alternative approach, based on experimental correlations such as Eq. (20), for the flowing supercooled surface film.

3.3. Prediction of unfrozen water layer runback

Once the mean velocity in the surface film is predicted by Eqs. (16) subject to (18) or (20), the mass flow rate of runback water can be determined. In particular, consider a control volume along the edge of the ice surface, thereby including ice, water and air phases, simultaneously (see Fig. 2). The respective phase fractions of ice, unfrozen water and air for the control volume centered about node i (subscript i) are $C_{s,i}$, $C_{l,i}$ and $1 - C_{s,i} - C_{l,i}$, respectively. The runback water is assumed to flow in the direction of the local external air velocity at node i, which is denoted by $V_{a,i}$. This air velocity is calculated from the Navier–Stokes solver in the freestream. Within the sub-control volume (SCV) containing the three-phase mixture, the height of the liquid film, b, can be estimated by the liquid phase fraction, $C_{l,i}$, multiplied by $2A/\Delta s$, where A and Δs refer to the SCV area and elemental side length, respectively (see Fig. 2).

Under these conditions, the following runback mass flow rate, $\dot{m}_i$, is obtained for the control volume centered about node i,

$$\dot{m}_i = \rho_w \bar{u}_{l,i} b = \rho_w \left(\frac{\tau_i b_i}{2\rho_w \nu_w} \right) b_i \tag{21}$$

where the subscript l refers to liquid (unfrozen water). A similar expression can be obtained for the other mass flow rate (denoted by $\dot{m}_{i+1}$) within the other SCV of the same finite element along the ice surface. This calculation raises an important feature of the runback flow algorithm, namely the two-dimensionality. In the previous heat transfer and momentum equations, variations in the direction parallel to the ice surface were not considered. However, in the context of the full numerical model, they represent a locally 1-D approximation within a given finite element. After all finite elements are assembled together, variations in both directions (including parallel to the ice surface) are predicted. For example, τ_i varies with $V_a(x, y)$ in Eq. (21). It is expected that the locally 1-D sub-element approximation is reasonable, particularly when the grid is sufficiently refined.

Once $\dot{m}_{l,i}$ and $\dot{m}_{l,i+1}$ are computed, these flows represent an inflow to a SCV, equal to the outflow (except opposite in sign) from the other SCV in the finite element along the ice surface (see Fig. 2). Consider the net flux across the sub-surface (SS) separating both of these SCVs. Then, the net mass transported across this SS over a time step, Δt, is

$$m_{l,r} = \left| \dot{m}_{l,i} - \dot{m}_{l,i+1} \right| \Delta t \tag{22}$$

where the subscript r refers to runback. After dividing by water density, this net mass flux can be expressed in terms of a volume of water. Then, dividing that runback volume by the SCV area (per unit depth), the resulting phase fraction of runback flow, $C_{i,\mathrm{r}}$, is determined.

In the numerical procedure, the liquid phase fraction was estimated previously, based on the mass influx of droplets and a heat balance involving non-solidified droplets. However, this fraction is now updated based on the runback flow, i.e.

$$C_{\mathrm{l},i} = \max[\min(C_{\mathrm{l},i} + C_{\mathrm{l},i,\mathrm{r}}, 1 - C_{\mathrm{s},i}), 0] \tag{23}$$

The max (maximum) condition is applied to ensure that the runback inflow cannot exceed the volume capacity of the SCV. Similarly, the min (minimum) condition is applied to ensure that the outflow does not remove more liquid than liquid available in the SCV. Once applied in this way, the runback flow can be predicted, after the phase fractions are determined based on incoming droplets from the external flow field. The extent of surface runoff is affected by the heat balance at the ice surface and Eq. (18). In particular, a limiting case occurs when the ambient air temperature decreases sufficiently to produce rime ice instead of glaze ice. In that case, no surface runoff is predicted, since $b_i \to 0$ when the liquid fraction approaches zero. The other limiting case occurs when no ice forms, as the air temperature exceeds the phase change point of water (0 °C). In that case, all incoming droplets flow off the surface due to runback.

Special consideration is required for convective upwinding of the droplet influx on the ice surface. For the external multiphase flow, a pressure-weighted upwinding is used to express the droplet flux at a sub-surface in terms of surrounding nodal values (Naterer, 2002b). These nodal values include both upstream and downstream influences. However, at the moving ice boundary, the downstream influence on incoming droplets should be removed since the solid ice surface is located downstream, rather than the droplet flow. As a result, pure upwinding of the droplet influx is performed in control volumes along the ice surface. For example, a non-zero ice fraction would be detected within a sub-volume of an element along the ice surface. Then, the upwinding coefficient at that sub-surface will not include any influence of the local node corresponding to that sub-volume, since that sub-volume is immersed in ice (or ice and unfrozen water layers, simultaneously). This approach permits impinging droplets at an oblique angle to the phase interface. Both the strength and directionality of the droplet influx is accommodated by calculating the component of droplet influx normal to the sub-surface of interest. In this way, the directional component of the upwinded velocities is used to determine the impinging droplet flux on the ice surface.

4. Results and discussion

In this section, validation of the previous numerical modelling will be performed through comparisons with analytical solutions and measured data. The first example involves incoming droplets and glaze ice growth on a planar surface, as depicted in Fig. 1. Since this example involves a high incoming velocity (90 m/s), it represents aircraft icing conditions rather than structural icing, such as icing of overhead power lines. The results will signify the reduced ice growth due to liquid runoff from the flowing supercooled surface film, in the direction perpendicular to the incoming velocity. Furthermore, they will signify the effects of parameters such as

air and surface temperatures, surface heating rate, and others. Although certain trends could be observed from the analytical solution (Myers and Hammond, 1999), this article's focus is presenting a numerical algorithm which could be applied to more complex geometries.

Aircraft icing usually involves higher air velocities with smaller droplet sizes than conditions encountered in structural icing. Extensions to the latter (structural icing) case would require modifications of Eq. (7), particularly the incoming droplet portion. For larger droplets (i.e., diameter of the order of a millimeter; power line icing), the kinetic energy contribution would likely arise at the ice/water interface, since the droplet impinges and passes through the thin liquid film without losing appreciable energy at the top of the water/air interface. In that case, when the droplets are larger or within the same order of thickness as the unfrozen liquid layer, they can essentially occupy the entire glaze film nearly instantaneously upon impact.

Although not explicitly outlined in the analytical solution, the numerical model must accommodate the two-dimensionality occurring from surface film runback in the direction perpendicular to the incoming air stream and droplets. The thickness of ice, $B(t)$, and the unfrozen water layer, $b(t)$, can be expressed by the following analytical solutions (Myers and Hammond, 1999):

$$\frac{\partial B}{\partial t} = \frac{a_2}{B} - \frac{a_3}{1 + a_1 b} \tag{24}$$

$$b = \frac{\beta \mathrm{VG}}{\rho_\mathrm{w}}(t - t_\mathrm{w}) - \frac{\rho_i}{\rho_\mathrm{w}}(B - B_\mathrm{w}) \tag{25}$$

where the variables t_w and B_w refer to the time and thickness of ice at the transition point from rime ice to glaze ice. Also, the constants a_1, a_2 and a_3 characterize the problem parameters, such as air temperature, air velocity and heat transfer parameters. Values of these parameters and constants are documented by Myers and Hammond (1999).

The surface runoff of unfrozen water can be determined from the difference between the dry growth limit and the predicted ice thickness from Eq. (24), since incoming droplets must either accumulate as ice, or flow off the ice surface. The analytical solution for the dry growth limit is derived by a balance between incoming droplets and corresponding ice growth. This solution follows from Eq. (25) with $b = t_\mathrm{w} = B_\mathrm{w} = 0$, i.e.,

$$\frac{\partial B}{\partial t} = \frac{\beta \mathrm{VG}}{\rho_i} \tag{26}$$

Then, the flow rate of surface runoff, $\hat{h}$, can be determined from the difference between rime ice, Eq. (26), and glaze ice, Eq. (24), as follows:

$$\frac{\partial \hat{h}}{\partial t} \equiv \left.\frac{\partial B}{\partial t}\right|_\mathrm{rime} - \left.\frac{\partial B}{\partial t}\right|_\mathrm{glaze} = \frac{\beta \mathrm{VG}}{\rho_i} - \frac{a_2}{B} + \frac{a_3}{1 + a_1 b} \tag{27}$$

where B and b represent the thicknesses under glaze conditions, as outlined in Eq. (24).

The main predicted parameters of interest in this problem are the growth of ice and the unfrozen water layer. Several grids were used, but relatively course grids (such as 5×21 nodes) were found to be adequate for providing the grid independent results. The example of a 5×21 grid layout refers to a uniform mesh spacing with 5 and 21 subdivisions in the x- and y-directions, respectively, with fewer x-direction subdivisions considered necessary since it is a 1-D problem in

the y-direction (see Fig. 1). Thus, the grid refinements were performed in y-direction, which corresponds to the direction of ice growth in this problem.

Wall boundary conditions of specified temperature and zero gradient of phase fraction were specified. The phase fraction condition means that the droplets initially enter a double control volume (CV) at the wall, until ice completely fills that CV. Then, the ice interface moves from CV to CV in the usual fashion. Icing researchers usually use n, when denoting the freezing fraction. At the inlet, all problem variables were specified for the boundary conditions. The inlet velocity and liquid water content were 90 m/s and 0.001 kg/m^3, respectively. Due to this high incoming velocity over a relatively short domain width (10 cm), and comparisons against a 1-D analytical solution, the multi-dimensional effects of droplets deflected by the airstream (including varying droplet sizes) are neglected. Also, a value of $E = 0.5$ is used in the computations, when comparing against the analytical solution having the same E value.

In Case 1 (Figs. 3–5), the ambient air and surface (wall) temperatures are $T_a = 272$ K and $T_s = 272$ K, respectively. Both temperatures are below the freezing point of water ($T_f = 273$ K). Thus, incoming droplets are partially solidified into ice on the wall, while some liquid flows off the surface as surface runback. Due to the difficulty of obtaining reliable, non-intrusive temperature measurements over a small thickness within the unfrozen water layer, there exists a lack of experimental data regarding temperatures therein. As a result, analytical solutions serve a useful role for validation of expected physical trends in the phase change predictions.

In Fig. 3, the predicted ice thickness is compared with the analytical solution and the dry growth limit for Case 1. Also, the curves corresponding to different collection efficiencies (labeled as variable E) are shown for comparison purposes. The collection efficiency refers to the ratio of impinging droplet influx to the mass influx that would occur on the surface if the droplets were not deflected by the air stream. The comparison with $E = 1$ in the dry growth limit is made for reference purposes, since it represents the maximum possible ice buildup when all incoming droplets are solidified immediately upon impact. The difference between the actual ice buildup and the dry

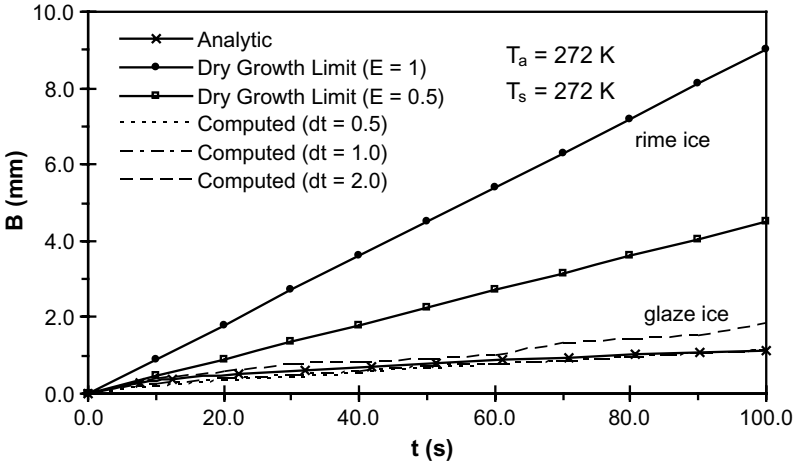

Fig. 3. Time step refinement study of predicted ice thickness (Case 1).

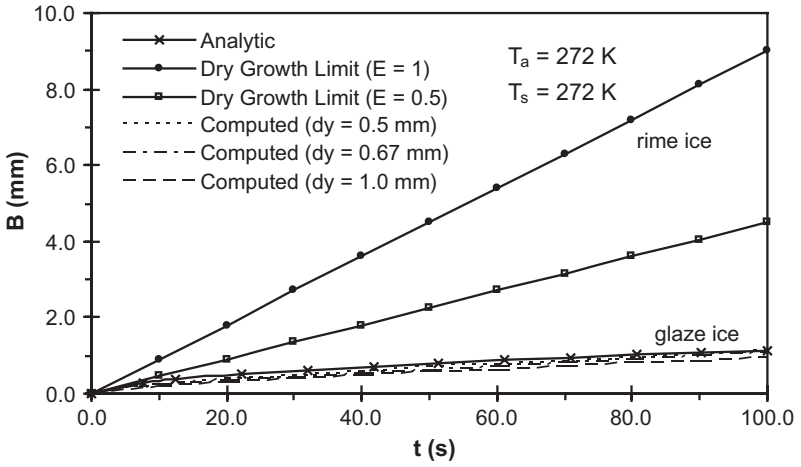

Fig. 4. Grid refinement study of predicted ice thickness.

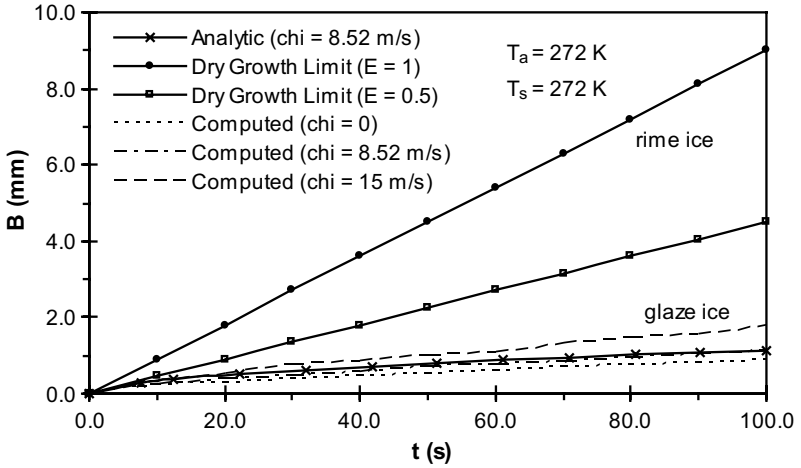

Fig. 5. Effects of evaporative heat transfer.

growth limit indicates the mass of liquid lost due to runoff or splashback from the surface. Surface runoff is predicted in the current formulation through Eqs. (8) and (23). The effects of splashback can be included therein, either directly modelled in the heat balances or indirectly through the collection efficiency. Although sub-grid modeling of droplet impingement is performed at the advancing ice interface, certain microscopic information involving splashback may be lost through the volume averaging process. Some examples include the detailed interactions of droplet collisions, coalescence or liquid sheared off from the surface of the unfrozen water layer by the air boundary layer. Detailed modeling of the collection efficiency with computational fluid dynamics (CFD) represents an important advance of current technology, beyond extensive empiricism which is often required in semi-analytical icing models.

As expected, the rate of rime ice buildup in Fig. 3 is greater than the glaze ice buildup, due to surface runoff of unfrozen water. The dry growth limit is shown for collection efficiencies of 1 and 1/2. In Fig. 3, it can be observed that the predicted results approach the analytical solution when the time step is reduced (note: dt refers to the time step size in seconds). When a discrete control volume becomes filled due to incoming solidified droplets, any excess mass must be transferred implicitly to adjacent volumes without any net loss of mass. This mass transfer varies with the size of the time step and mesh spacing, so establishing independence of these parameters is important for validating the algorithm for the moving phase interface.

Although close agreement with analytical results has been achieved with sufficiently refined mesh and time step sizes, some oscillatory behaviour is observed in the predicted results. This behaviour may be understood from the aforementioned excess mass transfer. A freezing fraction computed in Eq. (8) may render the surface film sub-divided among two adjacent control volumes when the ice interface is very close to the edge of a control volume. In that case, interpolation of temperatures in Eq. (8) could extend to six elements, rather than four elements surrounding one node when the interface movement stays within a single control volume during a time step. A control volume is defined by all sub-control volumes (SCVs) surrounding a given node (see Fig. 2). Thus, this extended interpolation may lead to certain inaccuracies, but results such as Fig. 3 indicate that the oscillations are reduced or eliminated when the mesh spacing and time step are reduced. In conventional methods of interface tracking, complex grid or coordinate transformations are often required. Avoiding these added computational costs, by the current method of volume averaging, is considered to outweigh the aforementioned inaccuracies for coarse grids or time steps.

A grid refinement study is illustrated in Fig. 4. It can be observed that the predicted results approach the analytical solution when the grid spacing is reduced. As mentioned earlier, the dry growth limits for different values of the collection efficiency are shown for comparison purposes, since they represent the maximum possible ice growth under the given flow conditions. Fig. 4 indicates that grid independence of the results was achieved. Additional grid sensitivity studies have been performed successfully, involving other problem variables and conditions. For example ($T_a = 253\ \mathrm{K} = T_s$), the difference between analytical and computed predictions of the ice growth rate varies by less than about 1% in the grid independent results. In the numerical formulation, the grid spacing is refined uniformly and special refinement is not required at the phase interface(s). This represents a useful advantage over interface tracking methods, which may require grid refinement near the moving boundary (phase interface) to apply the boundary conditions. For example, $k-\omega$ turbulence models require detailed grid refinement within the boundary layer (Wilcox, 1998). However, in our case, this would entail re-meshing after each time step due to the moving ice boundary. In contrast, the current formulation does not require such re-meshing, since sub-grid modeling of the interfacial mass, momentum and heat exchange is performed.

The time of departure of the glaze ice predictions from the dry growth limit represents the point of transition from rime ice to glaze ice. There exists a lack of detailed experimental data regarding this transition process, partly due to the difficulty of obtaining reliable non-intrusive measurements. Perturbations arising from impinging droplets, surface texture or other factors make detailed repeatability of such measurements difficult. Furthermore, the sensitivity of such results to empirical coefficients should not be overlooked. For example, only ±25% accuracy is available for

convective heat transfer coefficients of a cylinder in crossflow (Naterer, 2002c). The capabilities of any predictive icing models should be viewed within the context of these broad ranges of uncertainties. Thus, their main contributions are the capabilities of predicting the overall trends with reasonable accuracy.

The effects of evaporative heat transfer on the predicted ice growth are shown in Fig. 5. The analytical solution uses an evaporation coefficient (labeled as "chi" in Fig. 5) of $\chi_e = 8.52$ m/s (Myers and Hammond, 1999). The predicted results agree closely with that analytical result, based on a grid spacing and time step size of 0.5 mm and 1.0 s, respectively. These parameters were shown earlier to give time step and grid independent results. The predicted results indicate that errors in neglecting the evaporative heat loss ($\chi = 0$) are relatively minor. Evaporative cooling occurs when the air flows over the unfrozen water layer. Evaporation from the liquid surface involves a change of phase and the latent heat of vaporization. Water molecules near the surface of the glaze film experience collisions by surrounding gas molecules to increase their energy above the amount needed to overcome the surface binding energy. The energy absorbed to evaporate the liquid molecules largely comes from internal energy within the water layer, so that this water experiences a cooling effect (reduction of temperature) during the evaporation. Due to these effects, the relative importance of evaporative heat transfer is expected to vary between icing of aircraft (high air velocities, small droplets) and ground-based structures such as power lines (lower air velocities, larger droplets).

In this example, both convection and evaporation terms have comparable magnitudes since $\chi_e e_0 = 378.3$ W/m^2 K, so the evaporation coefficient is about 76% of the magnitude of the convective heat transfer coefficient, $h = 500$ W/m^2 K. Both coefficients are multiplied by ΔT ($= T_w - T_a$) to establish the full convection and evaporation energy terms, i.e., q_{conv} and q_{evap} in Eq. (8). Thus, both terms have approximately the same order of magnitude, but when compared against the other energy terms in Eq. (8), their relative importance varies depending on ΔT. When ΔT is small (Case 1; Fig. 5), the computed results confirm that errors in neglecting the evaporative heat loss are small, since its relative magnitude compared to the other energy terms is small. The effects of the evaporation term on the energy balance are considered to be relatively minor at low values of ΔT, such as Case 1 ($\Delta T = 1$ °C), but more significant at higher ΔT, such as Case 2 ($\Delta T = 10$ °C).

In Figs. 6–7, the non-dimensionalized results of ice thickness (B/B_e) and total volume of liquid runoff (per unit area of surface; h/h_e) are plotted against non-dimensional time, $t^* = (t - t_w)/(t_e - t_w)$. The purpose of using these non-dimensional variables is focusing on the glaze ice period, which is initiated at t_w. This extends over a reference time period denoted by t_e, when the ice thickness and liquid runoff are B_e and h_e, respectively. A grid spacing and time step size of 0.5 mm and 1.0 s, respectively, were used. The results show generally close agreement between analytical and computed results over a range of temperatures.

It should be noted that glaze ice is predicted under typical conditions representing in-flight aircraft icing at low temperatures. Low temperatures of −10 °C in Figs. 6–7 are often associated with rime ice on ground-based structures (Poots, 1996). However, the transition depends on the flow parameters, such as wind speed and droplet diameter. For example, larger supercooled droplets may tend to freeze more slowly as they spread over the surface to form an unfrozen water layer. Larger droplets and/or a high liquid water content have a potential for a high release rate of latent heat, thereby sustaining glaze ice at low temperatures.

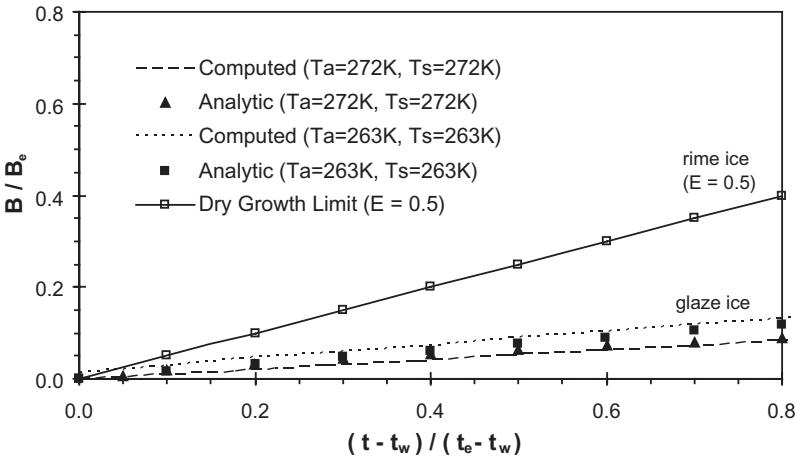

Fig. 6. Predicted ice thickness across a temperature range.

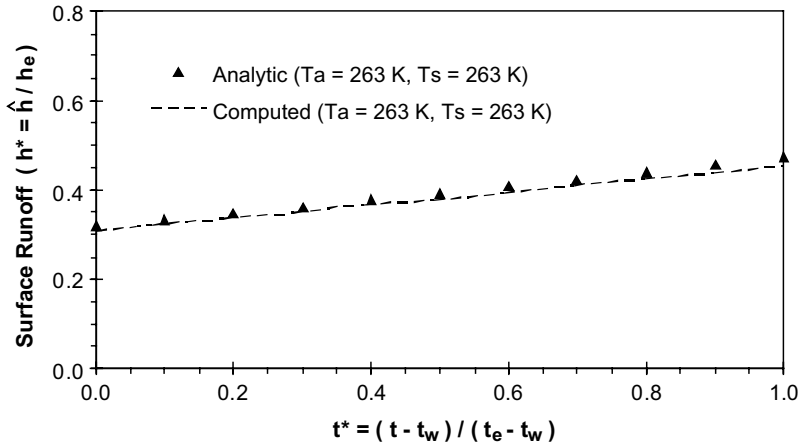

Fig. 7. Volume and rate of surface liquid runoff (Case 2).

As expected in Fig. 6, the rate of glaze ice growth is lower when the air and surface temperatures are reduced from −1 °C (272 K) to −10 °C (263 K). The rime ice thickness is zero initially. But the glaze ice results are slightly above zero initially ($t^* = 0$), since the non-dimensional time starts at t_w, which comes after the end of the rime ice period. As mentioned earlier, the computed results of Fig. 6 agree reasonably well with the analytical results.

In Fig. 7, the computed and analytical results are shown for Case 2 ($T_a = 263$ K and $T_s = 263$ K). The non-dimensional volume of liquid runoff (per unit area of surface) is determined from the difference between the dry growth limit and the predicted glaze ice buildup. This difference is caused by liquid runoff from the flowing supercooled surface film. The nearly constant slope of this curve indicates the volume flow rate of unfrozen water along the surface. In this article, this

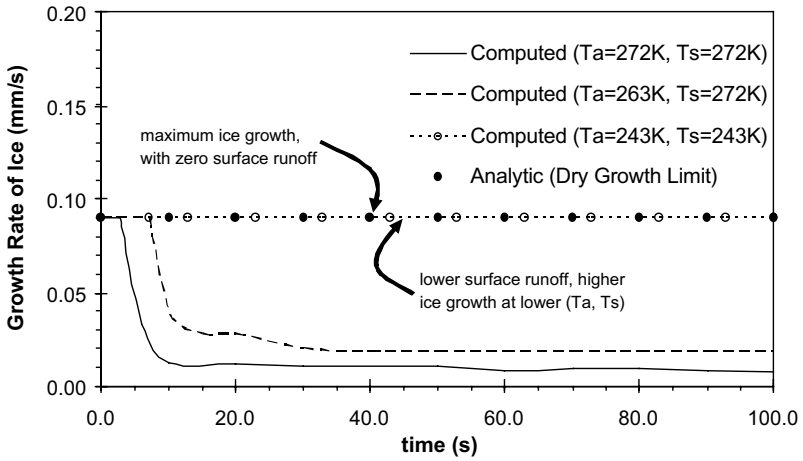

Fig. 8. Trends of ice growth rate with decreasing air temperature.

runback flow is driven by shear stresses imparted by the air flow across the water/air interface of the glaze film. Based on Sections 2.2 and 2.3, this runback flow is accompanied by a linear velocity profile through the thin surface layer of unfrozen water. In Fig. 7, it can be observed that the computed results of surface runoff agree closely with the analytical solution.

In Fig. 8, the predicted growth rate of ice over time is depicted, while considering a range of temperatures. The purpose of this figure is to confirm that this growth rate approaches the dry growth limit (0.09 mm/s) when the temperature is lowered sufficiently. In that case, the glaze ice must approach the two-phase limit (rime ice), since all droplets are solidified on impact. The sudden decrease of ice growth in the computed results at the early stages of time, which can be found analytically, reflects the transition from rime ice to glaze ice. Following this transition point, the surface runback leads to a lower growth of ice. It can be observed that the predicted results properly agree with the analytical solution (dry growth limit) at low air and surface temperatures. This result suggests that the freezing fraction of incoming droplets, Eq. (8), approaches the correct limiting value of 1 at low temperatures.

In the surface runoff modeling, Eqs. (17) and (21) are used to predict the runback flow. A main parameter of importance therein is the thickness of the unfrozen water layer, $b(t)$. In order to assess the suitability of such modeling in Eqs. (17) and (18), additional validation against experimental data for iced cables was performed in Fig. 9. The main purpose of Fig. 9 is to investigate the effects of water thickness on the growth of ice. The water thickness may vary due to waviness or splashback along its surface, or other factors. Figure 9 considers ±20% variations of the average water thickness due to such factors. These variations affect the temperature gradient and heat transfer across the water layer, thereby affecting the rate of ice growth.

The measured data was collected from freezing rain experiments described by Lu et al. (1999). Reaching proper thermal equilibrium between droplets and air, particularly over a wide range of droplet sizes and air temperatures, involves substantial practical difficulties. As a result, outdoor spray nozzles were used to simulate the freezing rain experiments essentially naturally. The air

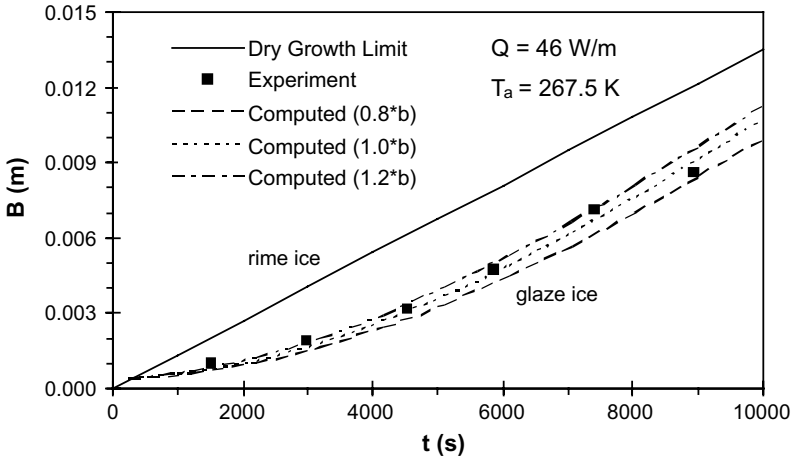

Fig. 9. Comparison between predicted and measured results (Case 3).

flow was driven past a horizontal, circular conductor placed perpendicular to the air stream. The supply water was pre-cooled and the distance of trajectory was sufficiently large, so that the droplets reached the test piece as close as possible to the air temperature. The measured ice mass was converted to an equivalent thickness of ice (depicted in Fig. 9), based on a uniform radial thickness which yields the same equivalent mass as that actually observed. Although not measured directly, the mass of unfrozen water must balance the difference between the measured ice growth and the total droplet influx on the surface. In the current technique, collecting the unfrozen water would be difficult due to uncontrolled mixing of surface runoff with other incoming droplets (not directly contacting the ice surface). Additional details of the experimental procedure are described by Lu et al. (1998).

In Fig. 9, the freestream wind velocity and liquid water content of air are 5 m/s and 0.00078 kg/m^3, respectively. The surface heating rate is 46 W/m and the ambient air temperature is $T_a = 267.5$ K. The results indicate that ±20% fluctuations in the water thickness still render results within close agreement of the experimental data. Thus, minor waviness and splashback, which alter the film thickness in Eqs. (17) and (18), are not expected to have a major impact on the ice prediction accuracy. However, much larger variations, such as those occurring from ice-induced surface vibrations (not modelled herein), would likely require extensions of the current numerical formulation.

The experimental uncertainties inherent in the measured data were caused by the measurement of the incoming precipitation, and other factors. The repeatability of this experimental data was confirmed. The data presented in Fig. 9 is considered to be accurate within ±10%. In addition to the results shown in Fig. 9, other comparisons with experimental data have been performed regarding the effects of heat conduction in the unfrozen water layer, and the temperature gradients on both sides of the ice/water interface. It was observed that when heat conduction was neglected through the water film, appreciable errors in the predicted ice thickness were observed under certain conditions.

5. Conclusions

A new fixed grid methodology has been developed for predicting multiphase flows with icing and impinging droplets on a flowing supercooled surface film. The finite element method indicates that phase volume averaging of the surface film can be used when analyzing the shear-driven motion of the film. Such averaging represents a useful alternative to Lagrangian phase tracking, when applied to one dispersed phase (droplet flow) and three continuous phases (air, surface liquid film and moving solid boundary), simultaneously. Mass transfer across the inter-element boundaries within the surface film, coupled with the momentum balance therein, can accommodate the liquid runback. By de-coupling these balances from the droplet influx, a standard algebraic solver can be used. This de-coupling is achieved through a volume averaged freezing fraction of incoming droplets. In the article, the predicted results are successfully validated against both analytical and experimental data.

Acknowledgements

The assistance and support provided by Dr. N. Popplewell (University of Manitoba), Mr. G. Venn and Dr. G. Richardson (GKN Westland Helicopters Ltd) are appreciated. Also, financial support from the Natural Sciences and Engineering Research Council of Canada is gratefully acknowledged.

Appendix A. Integral approximation of convection coefficient over a surface of arbitrary shape

The convective heat transfer coefficient can be approximated based on momentum and energy integral equations. The momentum integral equation represents a momentum balance across a laminar or turbulent boundary layer. For 2-D flows with an arbitrarily varying freestream velocity (Kays and Crawford, 1992)

$$\frac{\tau_w}{\rho} = \frac{d}{dx}\left(u_\infty^2 \delta_2\right) + \delta_1 u_\infty \frac{du_\infty}{dx} \tag{A.1}$$

where $\delta_1(x)$ is the displacement thickness,

$$\delta_1(x) = \frac{1}{u_\infty(x)} \int_0^\infty [u_\infty(x) - u(x,y)]dy \tag{A.2}$$

and δ_2 is the momentum thickness, given by

$$\delta_2 = \frac{1}{u_\infty^2} \int_0^\infty u(x,y)[u_\infty(x) - u(x,y)]dy \tag{A.3}$$

The velocity component along the surface in the x-direction is represented by $u(x,y)$.

A.1. Laminar regime

Based on the method of Thwaites (1949) for laminar flows, Eq. (A.1) can be solved to give

$$\delta_{2,l} = \frac{0.664 v^{0.5}}{u_\infty^{2.84}} \left(\int_0^x u_\infty(x)^{4.68}\, \mathrm{d}x \right)^{0.5} \tag{A.1.1}$$

A similar approximation for the energy integral equation yields (Kays and Crawford, 1992)

$$\frac{u_\infty}{v} \frac{\mathrm{d}(\delta_3^2)}{\mathrm{d}x} = 11.68 - 2.87 \frac{\delta_3^2}{v} \frac{\mathrm{d}u_\infty}{\mathrm{d}x} \tag{A.1.2}$$

where the conduction thickness, δ_3, is given by

$$\delta_3 = \frac{k(T_\mathrm{w} - T_\infty)}{q_\mathrm{w}} = \frac{k}{h(x)} \tag{A.1.3}$$

Eq. (A.1.2) can be integrated to give

$$\delta_3(x) = \left\{ \frac{11.68 v \int_0^x u_\infty^{1.87}\, \mathrm{d}x}{u_\infty(x)^{2.87}} \right\}^{0.5} \tag{A.1.4}$$

Thus, from Eq. (A.1.3), the convective heat transfer coefficient becomes

$$h(x) = 0.2926 k v^{-0.5} \left\{ u_\infty(x)^{-2.87} \int_0^S u_\infty(x)^{1.87}\, \mathrm{d}s \right\}^{-0.5} \tag{A.1.5}$$

A.2. Turbulent regime (smooth surface)

The power law of the wall for a turbulent boundary layer, together with the momentum integral equation, Eq. (A.1), can be used to give (Kays and Crawford, 1992)

$$\delta_{2,t} = \frac{0.036 v^{0.2}}{u_\infty(x)^{3.29}} \left(\int_0^x u_\infty(x)^{3.86}\, \mathrm{d}x \right)^{0.8} \tag{A.2.1}$$

Solving the energy integral equation for varying u_∞ and a smooth surface (Kays and Crawford, 1992),

$$St(x) = \frac{h(x)}{\rho c_p u_\infty(x)} = 0.0287 Pr^{-0.4} \frac{(T_\mathrm{w} - T_\infty)^{0.25} \mu^{0.2}}{\left[\int_0^x (T_\mathrm{w} - T_\infty)^{1.25} \rho u_\infty\, \mathrm{d}x \right]^{0.2}} \tag{A.2.2}$$

A.3. Turbulent regime (rough surface)

Based on the law of the wall for the thermal boundary layer along a rough surface,

$$St(x) = \frac{h(x)}{\rho c_p u_\infty(x)} = \frac{c_f/2}{Pr_t + \sqrt{c_f/2}/St_k} \tag{A.3.1}$$

$$\tau_w(x) = 0.0125\rho u_\infty^2 \left(\frac{\delta_2 u_\infty}{\nu}\right)^{-1/4} \tag{A.3.2}$$

where $Pr_t \approx 0.9$ (Kays and Crawford, 1992) and the friction coefficient, $c_f(x)$, is defined as

$$c_f(x) = \frac{\tau_w(x)}{\rho u_\infty^2/2} \tag{A.3.3}$$

Using the log law of the wall to represent the wall shear stress in Eq. (A.1), we have

$$\delta_{2,t} = \frac{0.036\nu^{0.2}}{u_\infty(x)^{3.29}} \left(\int_0^x u_\infty(x)^{3.86}\right)^{0.8} \tag{A.3.4}$$

The law of the wall for the fully rough region (Kays and Crawford, 1992) gives

$$\frac{c_f}{2} = \frac{0.168}{(\ln(846\delta_{2,t}(x)/k_s))^2} \tag{A.3.5}$$

where $\delta_{2,t}$ is determined from Eq. (A.3.4). The variable k_s is the specified grain roughness height. Also, St_k (Stanton number based on the friction velocity, $u_\tau = \sqrt{\tau_w/\rho}$) is required in Eq. (A.3.1), i.e.,

$$St_k = 0.8Re_k^{-0.2}Pr^{-0.44} \tag{A.3.6}$$

where

$$Re_k = \frac{u_\tau k_s}{\nu} \tag{A.3.7}$$

Based on these definitions, the appropriate regime can be determined as follows: $Re_k < 5$ (smooth), $5 < Re_k < 70$ (transition) and $Re_k > 70$ (rough). Then, the convective heat transfer coefficient can be computed based on the following steps: (i) find $\delta_{2,t}$ from Eq. (A.3.4), (ii) specify k_s and find $c_f/2$ from Eq. (A.3.5), (iii) find τ_w from Eq. (A.3.2) and use it to obtain Re_k and St_k in Eq. (A.3.6) and (iv) find $St(x)$ and $h(x)$ from Eq. (A.3.1). In the numerical model, the bounds of integration are the edges of the control volume at the ice interface.

References

Banerjee, S., Chan, A., 1980. Separated flow models—I. Analysis of the time averaged and local instantaneous formulations. Int. J. Multiphase Flow 6, 1–24.

Bourgault, Y., Beaugendre, H., Habashi, W.G., 2000. Development of a shallow water icing model in FENSAP-ICE. Journal of Aircraft 37, 640–646.

Cheremisinoff, N.P., Davis, E.J., 1979. Stratified turbulent—turbulent gas—liquid flow. AIChE Journal 25, 48–56.
Fulford, G.D., 1964. The flow of liquids in thin films. Advanced Chemical Engineering 5, 151–235.
Hansman, R.J., Yamaguchi, K., Berkowitz, B., Potapczuk, M., 1991. Modeling surface roughness effects on glaze ice accretion. AIAA Journal of Thermophysics and Heat Transfer 5.
Hedde, T., Guffond, D., 1992. Development of a three-dimensional icing code, comparison with experimental shapes. In: AIAA 30th Aerospace Sciences Meeting and Exhibit, January 6–9, Reno, NV, AIAA Paper 92-0041.
Hewitt, G.F., Shires, G.L., Polezhaev, Y.V., 1997. International Encyclopedia of Heat and Mass Transfer. CRC Press LLC.
Karev, A.R., Farzaneh, M., 2001. Freezing of flowing supercooled water film on an icing surface. In: Eastern Snow Conference 2001, 58th Annual Meeting, Ottawa, Canada, May.
Kays, W.M., Crawford, M.E., 1992. Convective Heat and Mass Transfer. McGraw-Hill, Inc.
Kind, R.J., 1998. Icing, frost and aircraft flight. Canadian Aeronautics and Space Journal 44, 110–118.
Langmuir, I., Blodgett, K.B., 1946. A mathematical investigation of water droplet trajectories, Army Air Forces Technical Report No. 541-8, February.
Lu, M.L., Popplewell, N., Shah, A.H., Barrett, W., Au, A., 1998. Mass of ice accretion from freezing rain simulations. In: Proceedings, 8th IWAIS, Reykjavik, Iceland.
Lu, M., Popplewell, N., Shah, A.H., Deng, H., Naterer, G.F., 1999. A semi-empirical icing model for an energized power line, Internal Report. Department of Mechanical and Industrial Engineering, University of Manitoba, Winnipeg, Canada.
Messinger, B.L., 1953. Equilibrium temperature of an unheated icing surface as a function of air speed. Journal of the Aeronautical Sciences 20, 29–42.
Myers, T.G., Charpin, J.P.F., Thompson, C.P., 2002. Slowly accreting glaze ice due to supercooled water impacting on a cold surface. Physics of Fluids 14, 240–256.
Myers, T.G., Charpin, J.P.F., 2000. The effect of the Coriolis force on axisymmetric rotating thin film flows. International Journal of Non-linear Mechanics 36, 629–635.
Myers, T.G., Hammond, D.W., 1999. Ice and water film growth from incoming supercooled droplets. International Journal of Heat and Mass Transfer 42, 2233–2242.
Myers, T., 1998. Thin films with high surface tension. SIAM Review 40, 441–462.
Naterer, G.F., 2002a. Energy balances at the air/liquid and liquid/solid interfaces with incoming droplets at a moving ice boundary. International Communications in Heat and Mass Transfer 29, 57–66.
Naterer, G.F., 2002b. Multiphase flow with impinging droplets and airstream interaction at a moving gas/solid interface. Int. J. Multiphase Flow 28, 451–477.
Naterer, G.F., 2002c. Heat Transfer in Single and Multiphase Systems. CRC Press, Boca Raton, FL.
Naterer, G.F., 2003. Eulerian three-phase formulation with coupled droplet flow and multimode heat transfer. Numerical Heat Transfer B 43, 331–352.
Poots, G., 1996. Ice and Snow Accretion on Structures. John Wiley and Sons Inc.
Szilder, K., Lozowski, E., Gates, E., 1987. Modelling ice accretion on non-rotating cylinders—the incorporation of time dependence and internal heat conduction. Cold Regions Science and Technology 13, 177–191.
Thwaites, B., 1949. Approximate calculation of the laminar boundary layer. Aeronautical Quarterly 1, 245–280.
Tsao, J.C., Rothmayer, A.P., Ruban, A.I., 1997. Stability of air flow past thin liquid films on airfoil. Computers and Fluids 26, 427–452.
Tsuboi, K., Kimura, S., 1998. Numerical study of the effect of droplet distribution in incompressible droplet flows. In: AIAA 29th Fluid Dynamics Conference, Albuquerque, NM, AIAA Paper 98-2561.
Van Driest, E.R., 1956. On turbulent flow near a wall. Journal of the Aeronautical Sciences 23, 1007–1011.
Wilcox, D., 1998. Turbulence Modeling for CFD, Second ed. DCW Industries Inc.